A New Semi-empirical Model of the Peak Electron Density of the Martian Ionosphere

Michael Mendillo[(1)], Angela G. Marusiak[(1)], Paul Withers[(1)], David Morgan[(2)], and Donald Gurnett[(2)]

1. Center for Space Physics, Boston University, Boston, Massachusetts, USA.
2. Department of Physics and Astronomy, The University of Iowa, Iowa City, Iowa, USA.

Corresponding Author: M. Mendillo, Center for Space Physics, Boston University, Boston, MA 02215, USA. (mendillo@bu.edu)

Key Points:

- Mars' peak electron density data used to make semi-empirical global model
- Mars ionosphere model extends from 1964 through 2019
- Mars ionospheric model available for upcoming NASA MAVEN mission

Abstract

Observations of the ionosphere of Mars have now reached a sufficient number to begin discussions on how best to create an empirically-based model of its global morphology. Here we use nearly 113,000 values of maximum electron density (N_{max}) obtained from 2005 to 2012 by the Mars Advanced Radar for Subsurface and Ionospheric Sounding (MARSIS) on board the Mars Express satellite. At the altitude of peak density, photo-chemical processes dominate over dynamical effects, and thus values of N_{max} can be organized using three basic parameters: Solar flux, solar zenith angle, and orbital distance. The model can be used retrospectively to provide N_{max} values for any date starting in 1965. Forecasts are possible using predicted solar flux values extending to the end of solar cycle 24. Validations using Viking *in situ* observations and radio occultation measurements from several satellite missions provide encouraging results for a useful semi-empirical climatological model.

Index Terms: Modeling and forecasting, ionization processes, Mars

Keywords: Mars, empirical modeling, ionosphere, MARSIS, MEX

1. Introduction.

The first-generation of observations of Mars' ionosphere, distributed over ~13 years (1965-1978, see Table 1 in *Mendillo et al*., [2003]), provided discovery-mode information about the vertical structure of the martian plasma environment. Yet, these initial data sets were far too sparse to be used as the basis for an empirical global model. The second-generation series of radio occultation experiments at Mars yielded a total of 5600 $N_e(h)$ profiles from the Mars Global Surveyor (MGS) satellite [*Hinson et al*., 1999], and a continuing series of profiles from the ESA's Mars Express (MEX) mission [*Pätzold et al*., 2005]. The science yield from these observations has been substantial, ranging from descriptions of basic morphology to disturbances associated with solar flares, meteor impacts, and crustal magnetic fields [see reviews in *Haider et al*., 2011; *Withers*, 2009]. The geometrical constraints associated with most of these radio occultation observations (high latitudes and high solar zenith angles) were still too restrictive for the specification of global morphologies.

The MEX satellite has a second radio science instrument, the Mars Advanced Radar for Subsurface and Ionospheric Sounding (MARSIS). MARSIS has two distinct modes of radar operations—an Active Ionosphere Sounder (AIS) [*Gurnett et al*., 2005] and a Sub-Surface (SS) radar mode [*Picardi et al*., 2005]. The former measures the electron densities down to the height of maximum electron density (N_{max}); the second mode obtains the integral of the full electron density profile, called the total electron content (TEC). MARSIS observations can, in principle, be conducted at any time or location, and very large databases of N_{max} and TEC are available to begin formulations of a global model of Mars' ionosphere.

2. Approach.

In this paper, we describe our attempt to construct a semi-empirical model (meaning numerical parameterizations, guided by theory, of observed patterns) of the martian ionosphere. The ideal approach would be to use observations of the full electron density profiles but, as described above, that is simply not possible from the limited distribution of samplings obtained from radio occultation methods. To create a baseline model of the martian ionosphere, we decided to focus initially on N_{max} as the parameter most descriptive of the magnitude of the ionosphere on any given day. This choice allows parameterizations of observed patterns to be approached using well-known and easily-available photochemical parameters. These include the Sun's irradiance reaching Mars (represented by the solar radio flux proxy, F10.7), and the solar zenith angle (SZA) at the orbital distance (*d*) of Mars on a specific day. Many previous studies have shown that N_{max} (e.g., *Němec et al*., [2011]) and TEC (e.g., *Lillis et al*., [2010]) at Mars follow these parameters, as photo-chemical theory demands.

A first attempt to create an observation-based model for Mars' ionosphere was presented in *Němec et al*. [2011] using the equations from basic Chapman Theory. In their formulation, attention was focused on altitudes at and above the height of N_{max}. Observations came from MARSIS/AIS, as well as *in-situ* plasma densities measured at the spacecraft altitude [*Duru et al*., 2008], between August'05 and December'09. Their focus was on defining correction factors to Chapman Theory's $N_e(h)$ profile parameters when observations were organized by their SZA and F10.7 values. Here we deal only with the peak electron density, and use the photo-chemical equilibrium equation for a

88 molecular ion/electron plasma, thus removing concerns about the inappropriate
89 assumptions within Chapman theory for the full electron density profile.

90 The MARSIS/AIS data archive now has 112,718 values of N_{max} spanning the years
91 2005-2012, thereby providing a more extensive set of observations (by a factor of ~3.5)
92 and a broader range of solar flux values than available at the time of the *Němec et al*.
93 [2011] study. It is this database that we use to create a semi-empirical ionospheric model
94 for Mars.

95 3. Method.

96 For each of the MARSIS N_{max} values, there is an associated UT date, solar zenith
97 angle (SZA), solar flux (F10.7), and distance from the Sun (*d* in AU). At the peak of the
98 ionosphere where the plasma frequency is determined, and the local electron density
99 represents a balance between production and loss, there is a simple radial dependence on
100 distance from the Sun (*d*), i.e., $N_{max} \sim 1/d$ [*Mendillo et al*., 2003]. The solar radio flux at
101 10.7 cm has long been used as a proxy for the EUV radiation responsible for N_{max}. While
102 direct measurements of solar irradiance at the appropriate wavelengths for photo-
103 ionization are now available, our initial choice in model development is to continue to
104 use F10.7 since it is available for both retroactive validations (to 1965) as well as for
105 predictions during the upcoming MAVEN mission (2014). F10.7 measurements at Earth
106 are routinely adjusted via $1/d^2$ to its value at 1 AU—thereby giving an index of pure solar
107 activity. Using these two well known radial dependences for photo-chemical processes,
108 the F10.7 solar fluxes at Earth and the MARSIS N_{max} data at *d* were adjusted to their
109 values at Mars' orbital mean distance (1.524 AU). In addition, the orbital longitude
110 separation of Mars from Earth are used to determine the terrestrial date most appropriate

111 (assuming solar rotation only changes) for the effective F10.7 to use at the time of an
112 observation at Mars. With these adjustment made, all of the N_{max} data were then sorted by
113 solar zenith angle and F10.7 at 1.524 AU. The results appear in Figure 1(a).

114 The pattern of N_{max} versus SZA and solar flux shown in panel (a) represents a new
115 aeronomic format for the portrayal of a molecular ion plasma in photo-chemical
116 equilibrium, and thus some initial discussion is needed. The coverage is obviously not
117 complete, but the highest values do appear where the SZA is small and the F10.7 is high
118 (shown by the bright yellow values). At high SZAs (top), the contours are essentially
119 horizontal for all solar fluxes—showing the rapid transitions to low N_{max} values that
120 occur when the SZA approaches 90^o (the dawn and dusk terminators). At low SZAs, the
121 pattern is quite different— the contours take on a more vertical appearance (as shown in
122 the dark green contour in the lower left)—indicating the daytime ionosphere getting
123 more robust as solar fluxes increase. With confidence thus established that the MARSIS
124 N_{max} morphology is consistent with basic photo-chemical equilibrium (PCE) theory, the
125 next step was to extend these partial trends in SZA and F10.7 to their full range of
126 possible values. The well-known PCE equation relating electron density to SZA and solar
127 flux via square-root dependences was weighted by the amount of data in each bin shown
128 in panel (a) to yield a smooth pattern for N_{max} at 1.524 AU, given by

129 $$N_{\max(SZA,Flux)} = 1.41 \times \frac{10^5 e^-}{cm^3} \times \left[\frac{Flux}{30} \times \cos(SZA)\right]^{1/2} \quad (1)$$

130 The results are presented in panel (b) of Figure 1. One can see a reasonable
131 representation of the partial pattern of data versus F10.7 and SZA in (a) by the full
132 dependence climatology shown in (b). We stress that the extension of the model to very

high solar fluxes is shown for illustration only; such conditions have been observed in the Earth's ionosphere but not yet at Mars.

4. Validation.

We first tested the model against individual measurements of N_{max} made by the Viking landers, and then with several radio occultation experiments spanning different levels of solar activity. In each case, the specific measurement date was used to determine the distance of Mars from the Sun. Then the solar rotation angle was found to relate the appropriate day for the F10.7 value observed at Earth (adjusted to 1 AU) to use at Mars' average distance (1.524 AU). The resulting N_{max} value for the SZA observed was then determined from panel (b) of Figure 1, as given by equation (1); it was then adjusted via a 1/d dependence to yield the model prediction. Table 1 gives the Viking-1&2 results together with a selection of radio occultation observations from several missions. In most cases, the model-data agreement is acceptable, if not excellent, while two cases (consecutive days) from the Mariner-9 mission show disagreements of 25-50%.

To quote uncertainty levels associated with the model we returned to the basic data set used to derive it. As pointed out in *Duru et al.* [2008], the plasma frequency can be measured by MARSIS/AIS with an accuracy of about ± 1%, and thus uncertainties in N_{max} are about ±2%. This is always less than the standard deviations about the mean values of N_{max} within the SZA-F10.7 bins shown in Figure 1(a). This prompted us to quote uncertainty ranges associated with the model using the observed σ (in percent) of the bin-by-bin mean values of N_{max} in Figure 1(a). As might be anticipated, the MARSIS σ(%) trend revealed a basic dependence upon the magnitude of N_{max}. Using quantitative groupings of peak density in units of 10^4 e^-/cm^3, we found that for $N_{max} > 16$, σ= 5%; for

156 $16 > N_{max} > 10$, $\sigma = 15\%$; for $10 > N_{max} > 4$, $\sigma = 20\%$ and for $N_{max} \leq 4$, $\sigma = 30\%$. These
157 are the origins of the $\sigma(\%)$ values in Table 1. To illustrate how the full rage of SZA
158 would lead to different uncertainties, we show in Figure 2(a) the case of the Viking-2
159 Lander. The abrupt changes in uncertainty come directly from the parameterization
160 described.

161 Panel (b) in Figure 2 shows results from the model's capability to predict N_{max} for a
162 future date: MAVEN's Mars Orbit Insertion (MOI), approximated as 15 September
163 2014. To make pure predictions, an estimate of solar flux is needed, which the model
164 takes from the NOAA predictions of monthly mean values for the remaining years of
165 solar cycle #24 (www.swpc.noaa.gov/SolarCycle/SC24). For the uncertainty levels to
166 associate with predictions, the model combines the uncertainties in F10.7 (130 ± 9.0)
167 with its parameterization of N_{max} variability (described above) to yield the somewhat
168 higher uncertainty limits shown for MAVEN's MOI date.

169 A different type of validation opportunity comes from the nearly continuous
170 observations made by the MGS radio occultation experiment from 1 Nov 2000 to 6 June
171 2001. This MGS "period-4" data set has the broadest span of SZAs (71.8^o-86.9^o), and
172 has been used in several previous studies summarized in *Haider et al.* [2011]. We ran the
173 model for each of the 1572 N_{max} observations, and the data-model comparisons are
174 shown in Figure 3. There is good agreement between the climatological model's peak
175 densities and the actual N_{max} values observed for most of the values below ~ $11x10^4$ e^-
176 $/cm^3$. To explore why the model over-estimates N_{max} above a certain threshold, we plot
177 in Figure 4(a) the same model-data comparisons in a time series format, with data shown
178 by gray dots and model results by the red dots. Panels (b) and (c) give the solar flux and

179 SZA at Mars at the same times. As pointed out when discussing Figure 1, the coupled
180 dependence of N_{max} upon SZA and F10.7 separates at the extremes of SZA: for high
181 SZA values (as with MGS period-4), SZA dominates; for low SZAs (not available from
182 MGS observations) solar flux dominates. Thus, the overall N_{max} morphology in the top
183 panel is due to the SZA pattern in the lower panel. The solar flux values are basically
184 constant at ~60 F10.7 units, except for short periods of solar variability. These include
185 periods of low flux (early Nov and Dec), and more dramatic cases of high flux (late Mar
186 and Apr). These are the points with maximum departures from the diagonal in Figure 3.
187 The lack of robust correlations between ionospheric densities and solar flux proxies is
188 a well-known statistical effect in terrestrial aeronomy. The linear correlations between F-
189 layer plasma and F10.7 (e.g., *Liu et al*., [2009]), and the quadratic correlation between E-
190 layer densities and F10.7 [*Titheridge,* 1997], break down when F10.7 exceeds ~170-180
191 units. This effect is often called "saturation"—meaning that observed values are lower
192 than predicted by high F10.7 values. Physically, it points out that F10.7 does not portray
193 the ionizing wavelengths (EUV and X-rays) correctly over their full range of possible
194 values [*Richards et al*., 1994]. For a semi-empirical model, a sudden increase in solar
195 flux value can appear as a solar maximum irradiance acting upon a solar minimum
196 background neutral atmosphere (thereby giving erroneous values). In reality, the
197 atmosphere also adjusts to higher solar fluxes, but not as instantaneously as photo-
198 ionization occurs. The F10.7 value of ~170 units at 1 AU corresponds to ~75 units at
199 Mars's mean distance, and panel (b) in Figure 4 shows this to be the case, i.e., the
200 "saturation" effect in Figure 3 is due to the inability of a semi-empirical model to handle
201 solar active regions. Solutions adopted in terrestrial aeronomy have been (a) to add a

202 constant to all F10.7 values thereby lessening the impact of high values [*Titheridge*,
203 1997], or (b) to average a daily F10.7 with its three-solar-rotation average [*Richards et*
204 *al*., 1994] to provide context for a specific daily value:

$$F_{effective} = \left[\frac{(F10.7)_{day} + < F10.7 >_{81-day}}{2}\right] \qquad (2)$$

205 Such a flux modification to our Mars model is shown by the blue dots in panel (a) of
206 Figure 4. The results are clearly in the correct direction, with the model's low values
207 being increased in Nov and Dec 2000, and its high values being decreased in Mar and
208 Apr 2001. While the maximum values from the model no longer exceed actual
209 observations, concerns remain, e.g., the time-lag in response seen in the data for late
210 March-early April, an effect not seen in the late April period; the model also
211 overestimates N_{max} during the rapidly changing SZAs in May-June. Within the context
212 of Figure 3, the equation (2) modification to the model results in the points at the lower
213 left of the plot being moved to the right, while those at the upper end move to the left—in
214 both cases falling closer to the diagonal. The formal statistic improvement in data-model
215 correlation using the Pearson correlation coefficients is from 0.88 to 0.91.

216 5. Summary.

217 We have used a database of over 100,000 observations of the peak electron density of
218 the ionosphere of Mars, spanning portions of solar cycles 23 and 24, merged with simple
219 photo-chemical theory, to develop a first-order global model of Mars' ionosphere. Future
220 validations and model improvements should include attempts to incorporate episodic
221 effects due to dust storms, solar active regions, energetic particles, and coronal mass
222 ejections. Additional challenges come from spatial sources of disturbance, e.g., crustal
223 magnetic fields and topological features. As with terrestrial aeronomy, day-to-day

variability driven by sources below the ionosphere (waves and tides) are the most difficult to include in a model.

The present version of our model is called the Mars Initial Reference Ionosphere (MIRI Mark-1); it is available as a resource to use and to test via an interactive web site (http://sirius.bu.edu/miri). Users simply input a date and MIRI generates a plot in the format shown in Figure 2 for either past or future dates. The authors welcome reports of model-data comparisons, as well as comments and suggestions on ways to proceed.

Acknowledgements: At Boston University, this work was supported, in part, by undergraduate student internship programs within the Center for Space Physics, by the comparative aeronomy component of NSF grant #1123222 (MM, PI), and by NASA MCDAP grant #NMX12AJ39G (PW, PI). Undergraduates Trey Wenger and Gerard Lawler created the MIRI website and helped with the validations, respectively. Clara Narvaez helped with manuscript preparation and submission. The MARSIS/AIS program at the University of Iowa was supported by NASA through contract #1224107 with the Jet Propulsion Laboratory.

References

Bougher, S., S. Engel, D. Hinson, and J. Forbes (2001), Mars Global Surveyor radio science electron density profiles: Neutral atmosphere implications, Geophys. Res. Lett., 28, 3091-3094, doi:10.1029/2001GL012884.

Duru, F., D. Gurnett, D. Morgan, R. Modolo, A. Nagy, and D. Najib (2008), Electron densities in the upper ionosphere of Mars from the excitation of electron plasma oscillations, J. Geophys. Res., 113, A07302, doi:10.1029/2008JA013073.

Fjeldbo, G., W. Fjeldbo and V. Eshleman (1966), Models for the atmosphere of Mars based on the Mariner 4 Occultation Experiment, J. Geophys. Res., 71(9), 2307-2316, doi:10.1029/JZ07li009p02307.

Gurnett, D., D. Kirchner, R. Huff, D. Morgan, A. Persoon, T. Averkamp, F. Duru, E. Nielsen, A Safaeinili, J. Plaut, and G. Picardi (2005), Radar sounding of the ionosphere of Mars, Science, 310, 1929-1933, doi:10.1126/science.1121868.

Haider, S., K. Mahajan, and E. Kallio (2011), Mars Ionosphere : A review of experimental results and modeling studies, Rev. Geophys., 49, RG4001, doi :10.1029/2011RG000357.

Hanson, W., S. Sanatani, and D. Zuccaro (1977), The Martian ionosphere as observed by the Viking retarding potential analyzers, J.Geophys. Res., 82, doi:10.1029/JS082i028p04351.

Hinson, D., R. Simpson, J. Twicken, G. Tyler, and F. Flasar (1999), Initial results from radio occultation measurements with Mars Global Surveyor, J. Geophys. Res., 104, 26,997-27,012, doi:10.1029/1999JE001069.

292 Kliore, A., G. Fjeldbo, B. Seidel, M. Sykes, and P. Woiceshyn (1973), S band radio
293 occultation measurements of the atmosphere and topography of Mars with Mariner
294 9: Extended mission coverage of polar and intermediate latitudes, J. Geophys. Res.,
295 78, 4331-4351, doi:10.1029/JB078i020p04331.
296 Lillis, R., D. Brain, S. England, P. Withers, M. Fillingim, and A. Safaeinili (2010), Total
297 electron content in the Mars ionosphere: Temporal studies and dependence on solar
298 EUV flux, J. Geophys. Res., doi:10.1029/2010JA015698.
299 Liu, L. W. Wan, B. Ning, and M.L. Zhang (2009), Climatology of the mean total electron
300 content derived from GPS global ionospheric maps, J. Geophys. Res., 114, A06308,
301 doi:10.1029/2009JA014244.
302 Mendillo, M., A. Lollo, P. Withers, M. Matta, M. Patzold, and S. Tellmann (2011),
303 Modeling Mars' ionosphere with constraints from same-day observations by Mars
304 Global Surveyor and Mars Express, J. Geophys. Res., 116, A11303,
305 doi:10.1029/2011JA016865.
306 Mendillo, M., S. Smith, J. Wroten, and H. Rishbeth (2003), Simultaneous ionospheric
307 variability on Earth and Mars, J. Geophys. Res., 108 (A12), 1432,
308 doi:10.1029/JA00996.
309 Němec, F., D. Morgan, D. Gurnett, F. Duru, and V. Truhlík (2011), Dayside ionosphere
310 of Mars: Empirical model based on data from the MARSIS instrument, J. Geophys.
311 Res., 116, E07003, doi:10.1029/2010JE003789.
312 Pätzold, M., S. Tellmann, B. Häusler, D. Hinson, R. Schaa, and G. Tyler (2005), A
313 sporadic third layer in the ionosphere of Mars, Science, 310, 837-839,
314 doi:10.1126/science.1117755.

315 Picardi, G., et al. (2005), Radar soundings of the subsurface of Mars, Science, 310
316 (5756), 1925–1928, doi:10.1126/science.1122165.
317 Richards, P., J. Fennelly, and D. Torr (1994), EUVAC: A solar EUV flux model for
318 aeronomic calculations, J. Geophys. Res., 99, 9981-8992.
319 Titheridge, J. (1997), Model results for the ionospheric E region: solar and seasonal
320 changes, Ann. Geophysicae, 15, 63-78.
321 Withers, P. (2009), A review of observed variability in the dayside ionosphere of Mars,
322 Adv. Space Res., 44, 277-307, doi:10.1016/j.asr.2009.04.027.
323
324
325
326
327
328
329
330
331
332
333
334
335
336
337

338 Figure Captions

339 Figure 1. (a) Maximum Electron density (N_{max}) of Mars' ionosphere portrayed on a
340 grid of solar zenith angle (SZA) and solar flux (F10.7) at Mars' mean orbital distance of
341 1.524 AU. (b) A photo-chemical equilibrium solution of N_{max} vs. solar flux and SZA
342 (Eqn 1, with flux = F10.7) normalized by the data bin with maximum observations (SZA
343 = 46^o, F10.7 = 30, N_{max} = 11.4 x 10^4 e^-/cm^3). Model predictions for high F10.7 are to
344 illustrate solar cycle effects

345 Figure 2. Examples of runs of the model for (a) a past date (the Viking-2 lander) and
346 (b) a future date (MAVEN's arrival at Mars). Both input and output parameters are
347 shown and the blue asterisk gives the N_{max} value at the SZA of the Viking-2 lander. The
348 uncertainty levels come from parameterizations of observed variabilities and, for
349 predictions, of solar cycle F10.7 uncertainties (see text).

350 Figure 3. Comparison of model results with MGS observations of N_{max} during a period
351 of nearly continuous observations (Nov 2000 – Jun 2001). For a climatological model,
352 agreement is acceptable except at the extremes of the diagonal line where the model
353 under-predicts low values and over-predicts high values (see text).

354 Figure 4. (a) Time-series of the data and model results given in Figure 3 with
355 simultaneous values of (b) F10.7 and (c) SZA at Mars. Data points are shown in gray,
356 with model results using equation 2 ($Flux=F_{effective}$) in blue. Light blue shading portrays
357 model uncertainties. The vertical dash-dot lines indicate the two time periods when F10.7
358 $\geq$ 75 units (see text).

359

360

361 Tables

362 Table 1. Summary of Model Predictions for Sample Data Sets.

Date	Mission	SZA	RF at 1AU	N_{max} observed ($10^4 e^-/cm^3$)	N_{max} Predicted ($10^4 e^-/cm^3$)
20 July 1976	Viking Lander 1[a]	43.5	70.2	10.3	10.3±1.6
3 Sept 1976	Viking Lander 2[a]	46.4	70.8	10.0	10.6±1.6
12 Dec 2004	MEX Radio Occultation[b]	83	95.6	5	5.3±1.1
12 Dec 2004	MGS Radio Occultation[b]	78	95.6	7.1	6.9±1.4
24 May 1972	Mariner 9[c]	76.3	162.8	9.9	9.2±1.8
7 June 1972		72.9	110.8	12	8.3±1.7
6 June 1972		73.2	114.3	10.4	8.4±1.7
13 June 1972		72.5	137.5	10.2	9.4±1.8
<1 January 2001>	MGS Radio Science[d]	<78.8>	170.9	8.5	8.4±1.7
14 June 1965	Mariner 4[e]	67	80.7	9.5	8.7±1.7

363 [a] *Hanson et al.*[1977], [b] *Mendillo et al.* [2011], [c] *Kliore et al.* [1973], [d] *Bougher et*

364 *al.*[2001], [e] *Fjeldbo et al.*[1966].

365

366

367

368

369

370

371

372

373

374

375

376 Figures

377

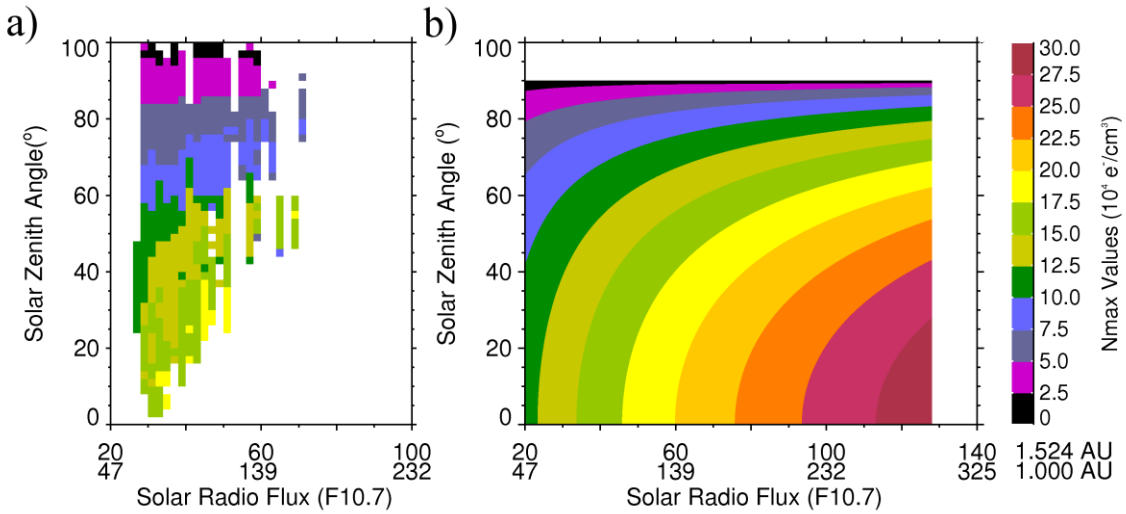

378

379 Figure 1.

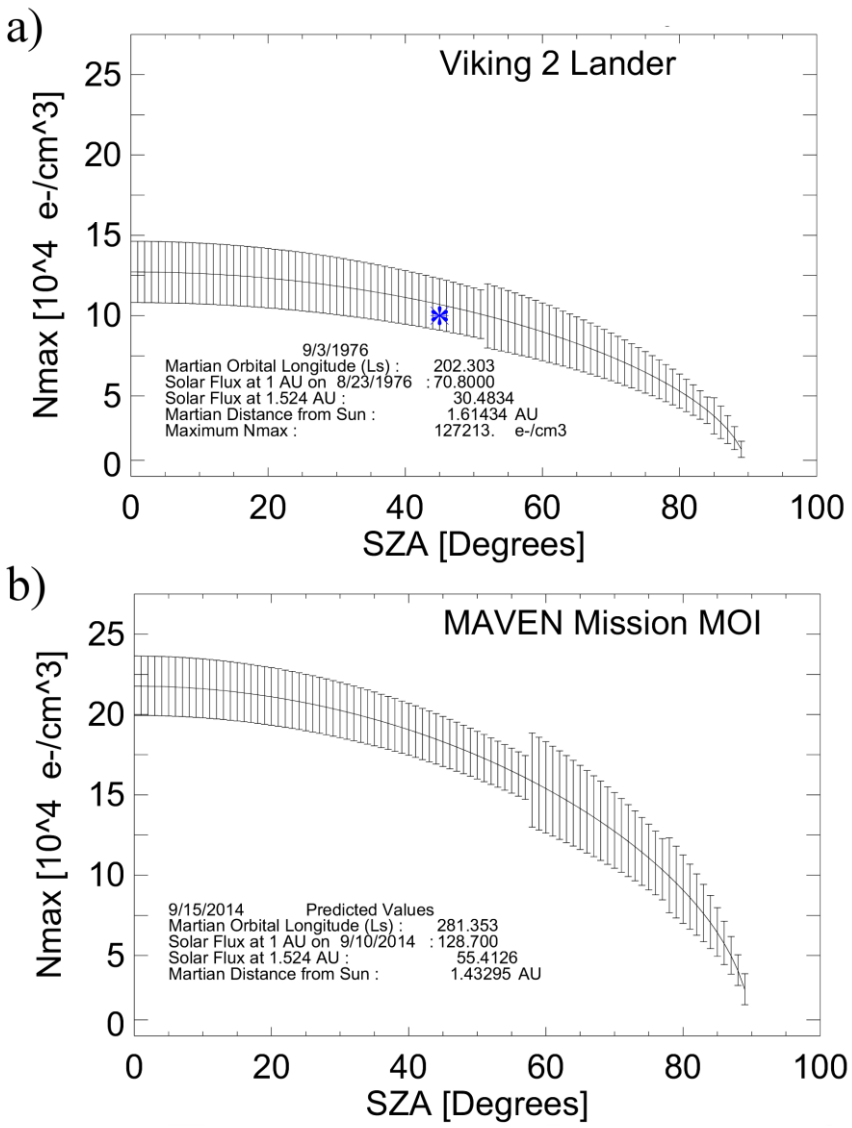

380

381 Figure 2.

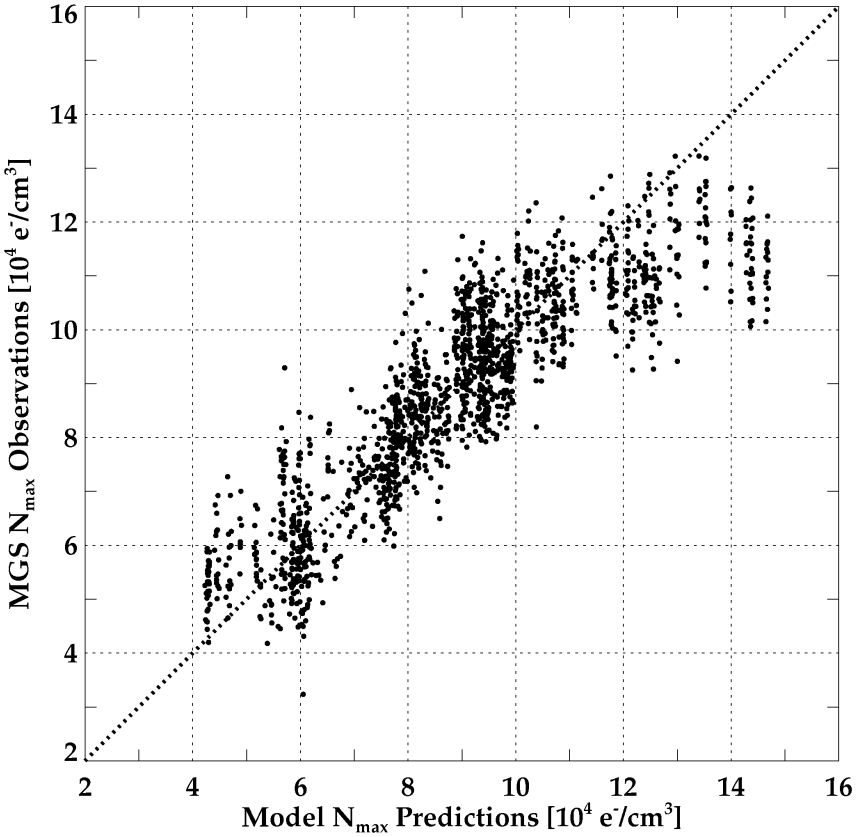

382

383 Figure 3.

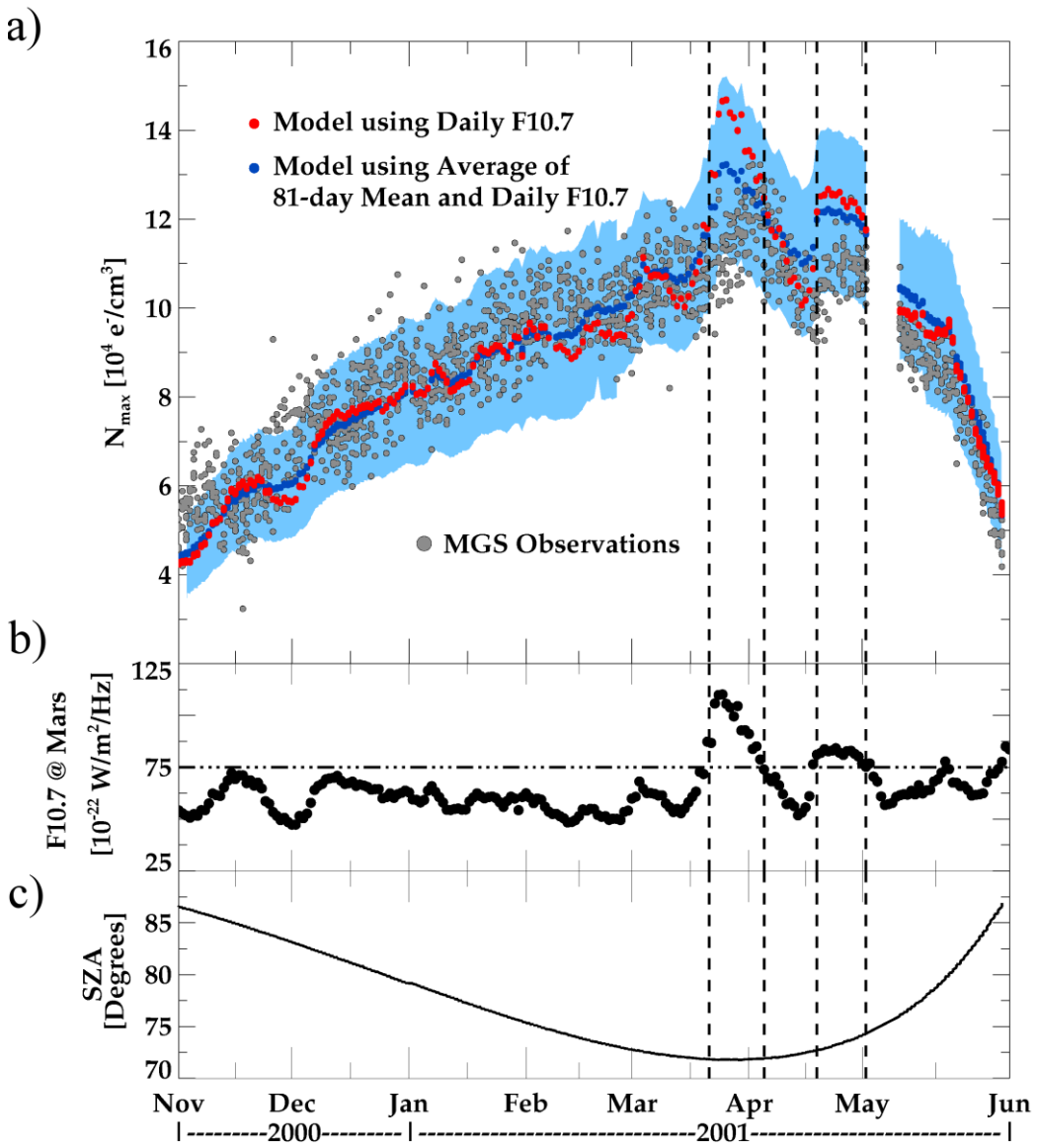

384

385 Figure 4.